Clim Dyn
DOI 10.1007/s00382-008-0484-5

30 and 43 months period cycles found in air temperature time series using the Morlet wavelet method

Samuel Nicolay · Georges Mabille · Xavier Fettweis · Michel Erpicum

Received: 27 June 2008 / Accepted: 14 October 2008

Abstract A wavelet-based methodology is applied to relevant climatic indices and air temperature records and allow to detect the existence of unexpected cycles. The scale spectrum shows the presence of two cycles of about 30 and 43 months, respectively, in the air–temperature time series, in addition to the well-known cycles of 1 day and 1 year. The two cycles do not affect the globe uniformly: some regions seem to be more influenced by the period of 30 months (e.g. Europe), while other areas are affected by the period of 43 months (e.g. North-West of the USA). Similar cycles are found in the indices and the regions influenced by these indices: the NAO index and the Western Europe display a cycle of 30 months, while the cycle of 43 months can be found in the ENSO index and in regions where it is known to have an impact.

Keywords Wavelet analysis · Climatic indices · Climate variability · Temperature cycles

1 Introduction

Climatic variations happen at all time scales, going from some hours to several milion years. The origins of these variations are often of complex nature, especially for small time scale events. Therefore, they represent a major barrier to the identification of the cycles induced by the natural climatic variability. The length of the reliable data time series is very short regarding the period of the most important, well known, climatological events (e.g. quaternary glaciations, little ice age and global warming) and the study of these time series regardless of these major climatic episodes is a knotty problem.

Numerous datasets (e.g. climatic indices, temperature data) allow to describe particular aspects of the climate; however, to our knowledge, no systematic spectral study has ever been performed. The high amplitude noise perturbing the signals and their non-stationary nature make the standard approaches (using e.g. Fourier transform) relatively ineffective. Paluš and Novotná (2006) have yet shown the existence of a cycle of about 30 months in records of monthly average near-surface air temperature from several European stations. These results were obtained using non-linear methods and statistical procedures. The emergence of recent mathematical tools and the fact that time series have reached respectable lengths (most of the records begin before 1950) allow the use of new deterministic techniques.

In this paper, we apply a wavelet-based method to obtain the spectra of climatic data and show the universality of some cycles. The main climatic and sun-related indices as well as several hundred weather stations were selected. The data are described in Sect. 2. The methodology is introduced in Sect. 3. In particular, we explain why the scale spectrum, used to compute the spectra, is able to show the existence of cycles in the analyzed data whereas other traditional methods are ineffective. The efficiency of the scale spectrum is validated on numerical examples. The results are exposed and discussed in Sect. 4. Two cycles (about 30 and 43 months, respectively) are observed in the climatic indices and in air temperature

S. Nicolay (✉)
Institute of Mathematics, University of Liège, Grande Traverse, 12, 4000 Liège, Belgium
e-mail: S.Nicolay@ulg.ac.be

G. Mabille · X. Fettweis · M. Erpicum
Institute of Climatology, University of Liège, Allée du 6 Août, 2, 4000 Liège, Belgium

records. Similar cycles are also found in the data related to the sun. Section 5 is devoted to the conclusions.

2 Short description of the data

In this section, we give a brief description of the data used in this study; the interested reader can consult the bibliography or the internet links to obtain more detailed informations. These records and the URL addresses where they can be retrieved are presented in Table 1. Unless explicitly mentionned, each data set runs from 1950 to 2007 (see also Sect. 3.4).

2.1 Air and sea surface temperatures

Global temperature reconstructions (*CRUTEM3gl*, *GLBTs*, *HadCRUT3gl* and *HadSST2gl*) using observations from several weather stations lead to time series taking into account either continental temperature only (*CRUTEM3gl* Brohan et al. 2006; Jones et al. 2001), sea surface temperature only (*HadSST2gl* Rayner et al. 2006) or continental and sea surface temperarture (*GLBTs* Hansen et al. 1999) and *HadCRUT3gl* (Rayner et al. 2006). *CRUTEM3vgl* is a variance adjusted version of CRUTEMP3gl.

Hemispherical temperature reconstructions are defined with the same records used in the global temperature recontrusctions, retaining hemispherical data only; a global temperature reconstruction ending with the suffix gl (gl stands for global) is splitted into two hemispherical temperature reconstructions, ending with nh (for Northen Hemisphere) and sh (for Southern Hemisphere), respectively. *GLBTs* is splitted into *NHTs* and *SHTs*.

The Air surface temperatures used have been obtained through the ECAD (Klein Tank et al. 2002) and GISS (Hansen et al. 1999) data sets.

The NCEP/NCAR reanalysis data set (Kalnay et al. 1996) is a continually updating gridded data set representing the state of the Earth's atmosphere, incorporating observations and global climate model output. In our study, only the air surface temperature data were selected.

2.2 Indices

The NAO indices caracterize the strenghth of the Westerlies. They are constructed from pressure differences

Table 1 Origin of the dataset used in this study

CRUTEM3	NOAA/OAR/ESRL PSD, Boulder, Colorado, USA	http://www.cdc.noaa.gov/
CRUTEM3v	NOAA/OAR/ESRL PSD,Boulder, Colorado, USA	http://www.cdc.noaa.gov/
HadCRUT3	NOAA/OAR/ESRL PSD, Boulder, Colorado, USA	http://www.cdc.noaa.gov/
HadCRUT3v	NOAA/OAR/ESRL PSD, Boulder, Colorado, USA	http://www.cru.uea.ac.uk/
HadSST2	Met Office, FitzRoy Road, Exeter,Devon, EX1 3PB, UK	http://badc.nerc.ac.uk/data/hadsst2/
GLBTs, *NHTs* and *SHTS*	Goddard Institute for Space Studies	http://data.giss.nasa.gov/
NCEP/NCAR reanalysis data V.1	NCEP/NCAR	http://www.cdc.noaa.gov/
Meteorological station data	European Climate Assessment Dataset (ECAD)	http://eca.knmi.nl/
GISS surface temperature analysis	Goddard Institute for SpaceStudies	http://data.giss.nasa.gov/
Bierset weather station (Belgium)	Belgian Air Component &Belgocontrol	
AO index CPC	National Weather Service, CPC	http://www.cpc.noaa.gov/
NAO index CPC	National Weather Service, CPC	http://www.cpc.ncep.noaa.gov/
NAO index CRU	Climatic ResearchUnit	http://www.cru.uea.ac.uk/
NOI	NOAA Environmental Research Division	http://www.pfeg.noaa.gov/
SOI	NOAA Environmental Research Division	http://www.pfeg.noaa.gov/
SOI*	NOAA Environmentfal Research Division	http://www.pfeg.noaa.gov/
PNA	National Weather Service, CPC	http://www.cpc.ncep.noaa.gov/
PDO Pacific decadal oscillation	Joint Inst. of the Study of the Atmos. and Ocean (JISAO)	http://jisao.washington.edu/
Global-SST ENSO index	JISAO	http://jisao.washington.edu
Multivariate ENSO index	NOAA EarthSystem Research Laboratory	http://www.cdc.noaa.gov/
EOF	JISAO	http://jisao.washington.edu/
QBO	CDC calculated at PSD	http://www.cdc.noaa.gov
Solar sunspot number	SolarInfluences Data Analysis Center (SIDC)	http://sidc.oma.be/
Daily sunspot region data	National Geophysical Data Center	http://www.ngdc.noaa.gov/
Solar flux	National Geophysical Data Center	ftp://ftp.ngdc.noaa.gov

between the Azores and Iceland (NAO CRU Hurrell 1995) or from the 500 mb height anomalies over the Northern Hemisphere (NAO CPC, Barnston and Livezey 1987).

The AO index (AO CPC, Zhou et al. 2001) is estimated from the 1,000 mb height anomalies poleward of 20N.

The NOI and SOI* indices (see Schwing et al. 2002) are characterized from the sea level pressure anomalies of the North Pacific (NOI) or South Pacific (SOI*), while the SOI index is constructed from the sea level pressue difference between Tahiti and Darwin.

The ENSO index (global-SST ENSO) is obtained from the sea surface temperature anomalies in the equatorial zone. The Multivariate ENSO index (MEI, Wolter and Timlin 1993; Wolter and Timlin 1998) is constructed using six different variables (sea-level pressure, the east–west and north–south components of the surface wind, sea surface temperature, surface air temperature and total amount of cloudiness).

The QBO index (see Baldwin et al. 2001) caracterize the equatorial wind blowing at 30 mb above Singapore.

The PNA and NP indices reflect the air mass flows over the North Pacific. The PNA index (Barnston and Livezey 1987) is defined over the whole Norther Hemisphere, while the NP index (Trenberth and Hurrell 1994) only takes into account the region 30N–65N, 160E–140W.

The PDO index (see Mantua et al. 1997; Zhang et al. 1997) is derived from the leading principal component of the monthly sea surface temperatures anomalies in the North Pacific Ocean, poleward of 20N.

2.3 Solar activity

The solar flux unit express the flux density of radio energy from the sun as received at the earth. The solar flux density is measured at a wavelength of 0.107 m.

The sunspot number represents the number of observed sunspots and sunspot groups on the solar surface.

The solar asymmetry is obtained from the following formula (Newton and Milsom 1955),

$$\frac{S_1 - S_2}{S_1 + S_2},$$

where S_1 is the sunspot number in the Northern Hemisphere and S_2 is the sunspot number in the Southern Hemisphere.

3 Methods of analysis

3.1 The continuous wavelet transform

Wavelet analysis is a mathematical technique first introduced by Goupillaud et al. (1984) and Kronland-Martinet et al. (1987) for analyzing seismic data and acoustic signals. It provides a two-dimensional unfolding of a one-dimensional signal by decomposing it into frequency and time coefficients. These coefficients are constructed from a function ψ, called wavelet, by means of dilatations and translations. The continuous wavelet transform turns a signal s into a function W:

$$W[s](t,a) = \int s(x)\bar{\psi}\left(\frac{x-t}{a}\right)dx/a,$$

where $\bar{\psi}$ denotes the complex conjugate ψ; the parameter $a > 0$ is the dilatation factor and t the time translation variable.

The wavelet must be integrable, square-integrable and satisfy the admissibility condition:

$$\int |\hat{\psi}(\omega)|^2/|\omega|d\omega < \infty,$$

where $\hat{\psi}$ denotes the Fourier transform of ψ, in order to allow the transform to be invertible. The last condition implies the cancellation of the first moment of ψ,

$$\int \psi(t)dt = 0;$$

this explains the denomination of wavelet, since a zero mean function has to oscillate.

The wavelet transform can be regarded as a mathematical microscope (for more details see for instance Arneodo et al. 1988), for which position and magnification correspond to t and $1/a$, respectively, the performance of the optics being determined by the choice of the wavelet. There are two main differences to the windowed Fourier transform. The scale a defines an adaptative window: the (numerical) support of the function $\psi(t/a)$ is smaller for higher frequencies. Moreover, one generally chooses a wavelet whose first m moments vanish, so that the associated wavelet transform is orthogonal to lower-degree polynomials, i.e. $W[s + P] = W[s]$, where P is a polynomial of degree lower than m. In other words, the wavelet transform is blind to lower-order polynomial behavior; in particular, linear tendencies do not affect the transform.

The continuous wavelet transform has been successfully applied to numerous practical and theoretical problems (the interested reader is referred to Arneodo et al. (1996, 2002), Daubechies (1992), Keller (2004), Mallat (1999) or Meyer (1989).

3.2 A wavelet-based spectrum: the scale spectrum

The Morlet wavelet is particularly well conditioned for frequency-based study. The Morlet wavelet, as defined by Kronland-Martinet et al. (1987), is a function ψ satisfying the equality

$$\hat{\psi}(\omega) = \exp\left(-\frac{(\omega-\Omega)^2}{2}\right) - \exp\left(-\frac{\omega^2+\Omega^2}{2}\right),$$

where Ω is a constant called the central frequency. If $\Omega > 5$, we can neglect some error terms and claim that the function belongs to the second complex Hardy space, i.e. $\hat{\psi}(\omega) = 0\ \forall \omega < 0$. For such a function, we have

$$W[\cos(\omega_0 t)](t,a) = \exp(i\omega_0 t)\hat{\psi}(a\omega_0), \quad (1)$$

so that the frequency ω_0 is given by the maximum of $\hat{\psi}(a\omega_0)$, which is $a_\omega = \Omega/\omega_0$. Consequently, the unknown frequency ω_0 can be obtained through the maximum a_ω of $|W[cos(\omega_0 t)]|$, since we have $\omega_0 = \Omega/a_\omega$. The frequencies composing a signal can be obtained with such a method, using the linearity of the wavelet transform.

There are many ways to define a wavelet spectrum. The one we present here is based on the preceding remark. The scale spectrum of a signal s is, following Nicolay et al. (2004),

$$\Lambda(a) = E|W[s](t,a)|,$$

where E denotes the mean over time t.

As we will see in Sect. 3.3, the main advantage of the scale spectrum is its ability to detect "pseudo frequencies": if ω_0 is replaced by a smooth function of t, $v(t)$ with

$$\frac{d}{dt}v(t) \ll 1, \quad Ev(t) = \omega_0,$$

the strong coefficients that were located near a_ω will be spread in a neighborhood of a_ω. For such a drifting frequency, the bump corresponding to ω_0 in the scale spectrum Λ is thus widened.

Let us end this paragraph with some remarks. If s is a self-similar signal with exponent H, i.e. if $s(a\ t) = a^H\ s(t)$, where the equality holds in some sense, the quantity

$$E\left|W\left[\frac{d}{dt}s\right](t,a)\right|$$

should behaves like Ca^{H-1}, where C is a constant. In particular, the long-range correlation exponents of a colored Gaussian noise can be estimated through a linear regression over logΛ. Finally, let us recall that, since the wavelet transform is orthogonal to lower-degree polynomials, linear tendencies do not affect the scale spectrum.

3.3 Numerical examples

The efficiency of the scale spectrum can be simply illustrated on numerically generated test data.

To simulate the influence of the cycle of 1 year in the daily-sampled air temperature data, let us set

$$v_1 = \frac{2\pi}{365.25}$$

so that the function

$$f_1(t) = 8\cos(v_1 t) \quad (2)$$

is periodic of period 1 year. The size of the signal we are working with is equal to $S = 21{,}200$ (about 58 years). As shown in Fig. 1a, the associated scale spectrum Λ_1 clearly displays a maximum at a position corresponding to a period of 1 year; the associated amplitude is $\Lambda_1(a_1) = 8$.

If a period of 30 months of smaller amplitude is added, i.e. if we set

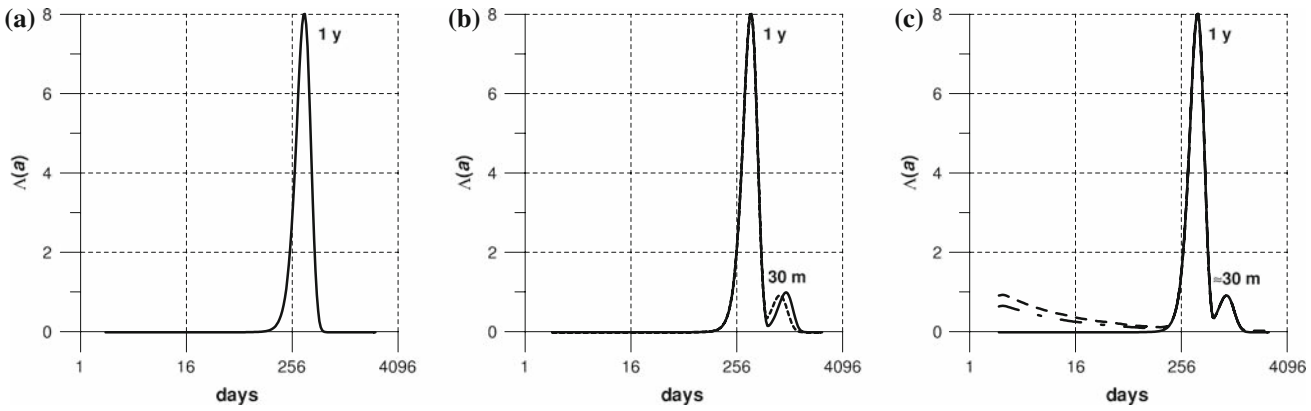

Fig. 1 Scale spectra of synthetic signals. **a** Spectrum of a signal simulating a period of one year in daily-sampled air temperature time series (see equality 2). **b** Spectrum of a signal simulating a period of 1-year and a period of 30 months (*solid lines*, see equality 3), or a pseudo period ranging from 26 to 30 months (*dashed lines*, see equality 4). **c** If a Gaussian noise (lines of type – - – represent the spectrum obtained after the addition of a standard Gaussian noise (see equality 5); lines of type (– –) represent the spectrum obtained after the addition of a Gaussian noise with variance $\sigma^2 = 2$) is added, one obtains a spectrum with a power–law behavior. Finally, the scale spectrum is left unchanged if tendencies are added (see equality 6)

$$f_2(t) = 8\cos(v_1 t) + \cos(v_2 t), \quad (3)$$

with

$$v_2 = \frac{2\pi}{365.25}\frac{1}{2.5},$$

a second maximum is detected in the associated scale spectrum Λ_2 at a position corresponding to 30 months (see Fig. 1b). One also gets an amplitude equal to $\Lambda_2(a_2) = 1$. As shown in Fig. 1b, this maximum is widened if we replace the period v_2 with a "pseudo period"

$$\gamma_2(t) = v_2\left(1 + \frac{t}{6S}\right). \quad (4)$$

Such a modification induces a variation of the original period, ranging from 26 to 30 months.

The positions of the maxima are kept unchanged if a standard Gaussian noise n is added, i.e. if we set

$$f_3(t) = 8\cos(v_1 t) + \cos(\gamma_2(t)t) + n(t) \quad (5)$$

(see Fig. 1c) or even $f_3 = f_2 + 2n$. Finally, one can illustrate the fact that the scale spectra is blind to tendencies by showing that $\Lambda_3 = \Lambda_4$, where

$$f_4(t) = f_3(t) + \frac{4t}{1,000} + 10 \quad (6)$$

(see Fig. 1c).

These examples show that we can detect (pseudo) periods close to 30 months without considering the existence of tendencies or Gaussian noise. However, let us remark that longer periods could be out of range of our methodology because of the small size of the data at our disposal.

3.4 Some remarks about the application to climatic data

Before applying systematically the scale spectrum to climatic data, some remarks must be done.

- The length of a period that can be detected using the scale spectrum obviously depends on the size of the analyzed signal. More precisely, the longest observable period depends on the maximum scale that can be computed, which is proportional to the logarithm of the size of the signal. For example, when working with a daily-sampled signal, 10 years of data allows to recover periods of length up to 7.5 months, while 20 years of data allows to recover periods up to 1.5 years. Again, covering 30 years is sufficient to obtain periods of length lower than 3 years, but lengthier periods can only be reached if the data covers at least 55 years.

Unless explicitly mentioned, all the data have been systematically truncated so that the starting year is 1950. This year has been chosen in order to be able to reach periods of length up to 5.6 years and keep a sufficiently large number of signals in the data set. Moreover, data from the pre-1950 period are often missing or sparse and less reliable.

- As expected, the scale spectrum allows to recover some well-known cycles. Figure 2 shows the scale spectrum of the Bierset (50°39′, 5°27′, 186 m, Belgium) air temperature records (see Table 1). These data are hourly-sampled. One clearly sees two maxima located around 1 day and 1 year, respectively. Looking at the amplitude of the first one allows to roughly estimate the contribution of the cycle of 1 day: the total variation of the temperature induced by this cycle is about two times the maximum, i.e. 5.2°. For the cycle of 1 year, one gets 15.5°. A direct estimation confirms these results: when fitting the temperature records series s with the signal

$$\tilde{s}(x; c_1, c_2, \phi_2, \phi_2) = c_1 \sin(2\pi x/24 + \phi_1) + c_2 \sin(2\pi x/8,766 + \phi_2) + Es,$$

using the downhill simplex method (see Nelder and Mead 1965), one gets $2c_1 = 5.3$ and $2c_2 = 15.4$. One also clearly observes the existence of a maximum near 30 months, contributing for a variation of 0.8°. This observation will be discussed afterwards.

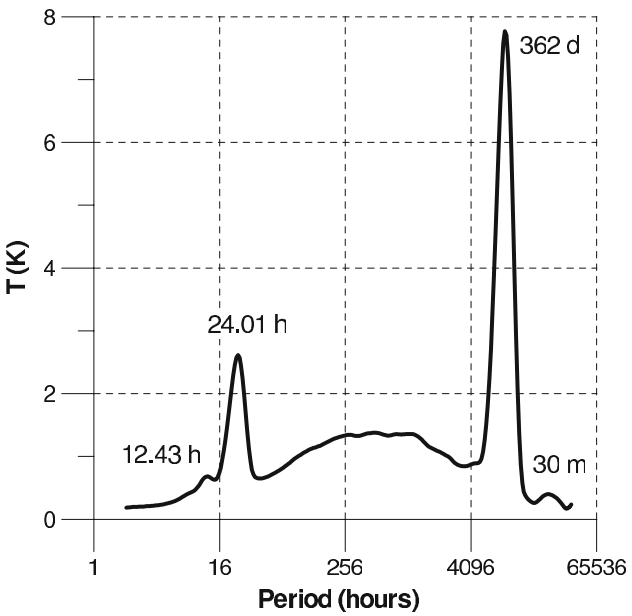

Fig. 2 The scale spectrum of the Bierset air temperature data (the signal is hourly-sampled). The abscissa are in logarithmic scale; the starting year is 1966. The main peak corresponds to the cycle of 1 year and the second one to the cycle of 24 h. Another maximum, corresponding to a cycle of approximatively 30 months is also observed

- The precision of the detected cycles of period longer than 30 months in the climatic data can be roughly evaluated as follows: for a given signal s, one computes the signal $s' = s + n$, where n is a centered Gaussian noise with a variance equal to twice the variance of s. The scale spectrum Λ' of s' is then calculated and the maxima of Λ' are compared to those of the spectrum Λ of s. This comparison has been systematically done for 10^6 realizations of s'. For daily-sampled data, 96% of the spectra Λ' display the same maxima as Λ with an error lower than 3 months. In particular, for the signals related to the NAO and ENSO indices, 96% of the spectra Λ' display the same maxima with a precision of 2 months. Subsequently, we will implicitly suppose that the precision on the detected cycles is 3 months.

4 Results

4.1 Scale spectra of temperature records

Global Series As illustrated in Fig. 3, the shape of the scale spectra obtained from global temperature data (*CRUTEM3gl* and *CRUTEM3vgl*) clearly shows two extrema corresponding to the existence of two cycles: $c_1 = 30 \pm 3$ months (hereafter denoted c_1) and $c_2 = 43 \pm 3$ months (hereafter denoted c_2). The second cycle is also found in the scale spectra of series where the sea surface temperature (SST) is taken into account (namely *HadCRUT3*, *HadCRUT3v* and GLBTs), while the maxima corresponding to the first cycle is not so well shaped for such series. The scale spectra obtained from the series of the SST (HadSST2) still clearly displays the cycle c_2, while the cycle c_1 is hardly seen.

Series depending on the hemisphere The scale spectra associated to the global temperature time series in the Northern Hemisphere also display a maximum near 30 months (see Fig. 4). This cycle is more clearly seen when considering series where the SST are not taken into account (*CRUTEM3nh* and *CRUTEM3vnh*), while it is fading to the benefit of the cycle c_2 for the series *HadCRUT3* and *HadCRUT3v*; c_1 is hardly seen for the series NHTs and *HadSST2*. The scale spectra related to the global temperature time series in the Southern Hemisphere show a dominating bump near c_2, while the cycle c_1 is less marked (see Fig. 5). Indeed, for *HadCRUT3sh*, *HadCRUT3vsh* and *HadSST2sh*, the observed cycle that is the closest to c_1 is shorter (about 25 months). When considering the scale spectrum of the series SHTs, the cycle of about 30 months is as marked as the cycle of 43 months.

Since, most of the continents are situated on the Northern Hemisphere, the observation of the global and hemisphere-dependant time series seem to show an influence of the continents on the cycle c_1 and an influence of the oceans on the cycle c_2. However, let us remark that since only a small number of stations is taken into account to build these records, the above comment must be taken with circumspection and no conclusion can be drawn.

Temperature times series obtained from meteorological stations The scale spectra of a hundred of temperature time series have been computed using ECAD and GISS Surface Temperature Analysis data. Only the most complete data have been chosen. The observations of the related scale spectra confirm the existence of the two cycles mentioned above.

The cycle c_1 is observed for every station in Europe, but also in Asia, North America, South India, Sri Lanka, Thailand, Malaysia, Australia and Japan. This cycle is also detected in South America: in Patagonia and in the region of Belem, in Brazil (see Fig. 6).

These results are in good agreement with the statistical approach used by Paluš and Novotná 2006); these authors use a non-linear method based on a red noise model to test

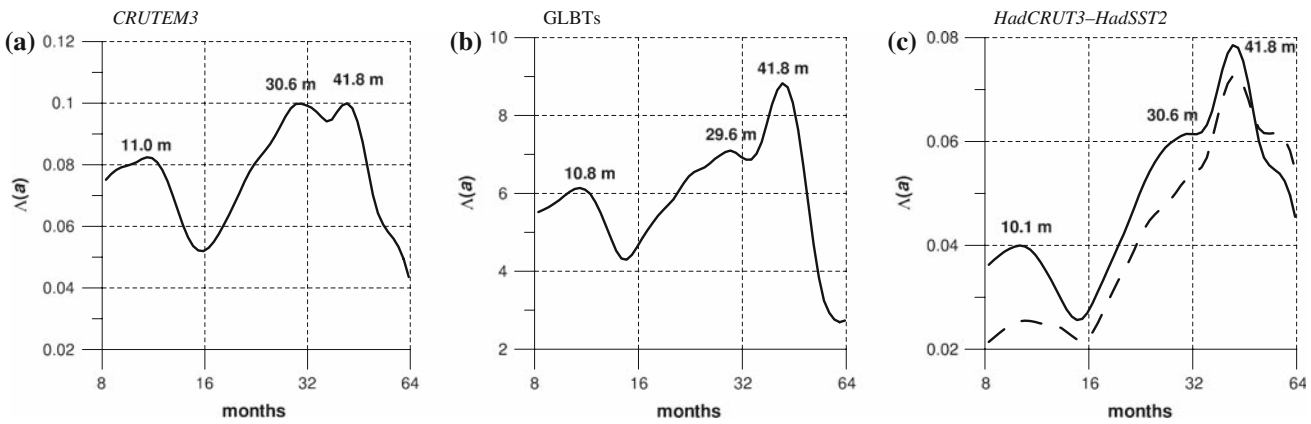

Fig. 3 Scale spectra of global temperature records. **a** *CRUTEM3*. **b** GLBTs. **c** *HadCRUT3* (*solid lines*) and *HadSST2* (*dashed lines*)

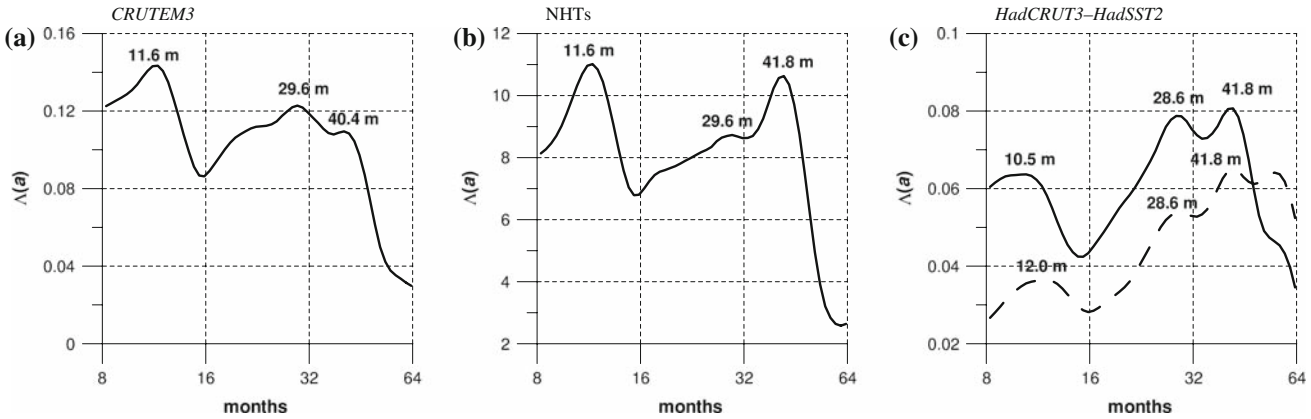

Fig. 4 Scale spectra of Northern Hemisphere temperature records. **a** CRUTEM3. **b** NHTs. **c** HadCRUT3 (*solid lines*) and HadSST2 (*dashed lines*)

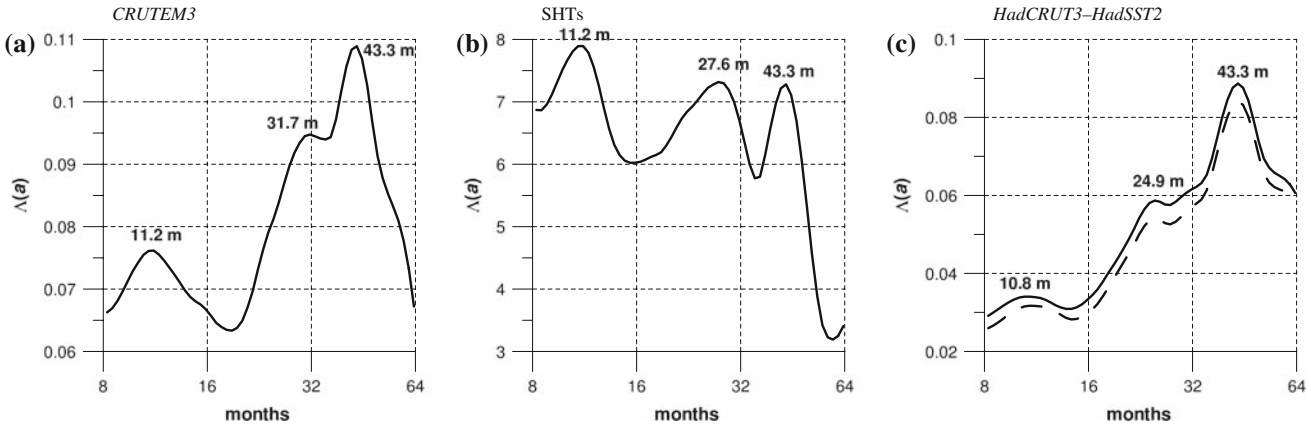

Fig. 5 Scale spectra of Southern Hemisphere temperature records. **a** CRUTEM3. **b** SHTs. **c** HadCRUT3 (*solid lines*) and HadSST2 (*dashed lines*)

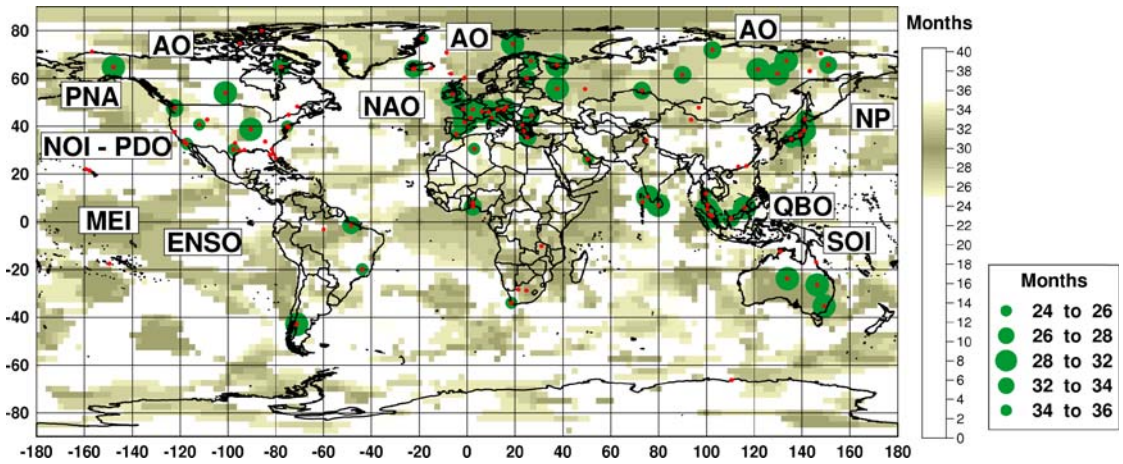

Fig. 6 NCEP/NCAR reanalysis. The regions on the globe where the cycle c_1 has been detected on the grid nodes are colored using a color palette going from white (if no cycle is detected) to khaki (corresponding to c_1). Weather stations have been superimposed on the map using *red dots*. If c_1 is observed in a temperature time series, the corresponding station is circled in *green*, with a radius depending on the difference between 30 months and the detected period (the larger circles correspond to the smallest difference). The main locations linked to the indices are also represented on the map

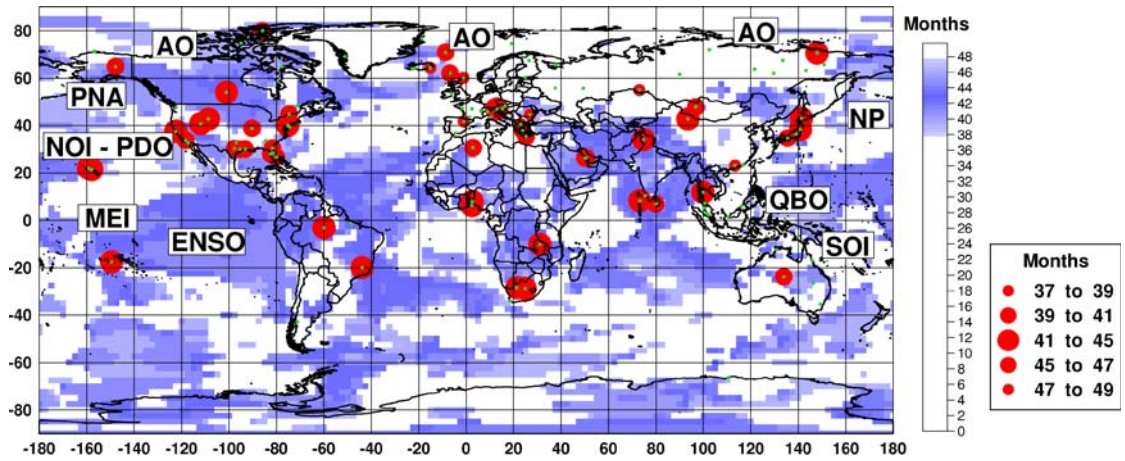

Fig. 7 NCEP/NCAR reanalysis. The regions on the globe where the cycle c_2 has been detected on the grid nodes are colored using a color palette going from white (if no cycle is detected) to blue (corresponding to c_2). Weather stations have been superimposed on the map using green dots. If c_2 is observed in a temperature time series, the corresponding station is circled in *red*, with a radius depending on the difference between 43 months and the detected period (*larger circles* correspond to the smallest difference). The main locations linked to the indices are also represented on the map

the hypothesis of the existence of periods in the records of monthly average near-surface air temperature in Central Europe and detect a cycle similar to c_1.

The cycle c_2 is seen in different regions on the globe: in Africa, North America, in the North Atlantic islands, Spain, Brazil, South India, Malaysia, Thailand and Japan (see Fig. 7).

The influence of the SST seems to influence the temperatures at the stations on the continents of the Southern Hemisphere, since cycles with the same period are detected.

The total variation of temperature associated to one of the cycles c_1 or c_2 ranges from 0.4 to 1.4°.

NCEP/NCAR reanalysis, surface temperature The surface temperature from NCEP/NCAR reanalysis have been used in order to compute the scale spectra on a 2.5 ° × 2.5 ° global grid. As illustrated in Figs. 6 and 7, the analysis of the so-obtained spectra leads to the same conclusions: the area where the cycle c_1 (resp., c_2) is detected covers the station where this cycle has been observed in the air–temperature time series. Each model grid point displays at least one of these two cycles.

4.2 Scale spectra of atmospheric indices

The next step is to link the area affected by one of the two detected cycles with the factors that influence the air temperature in these regions. The advection of air mass flows influences the air temperature measured at the meteorological stations. These movements, and their consequences to the air temperature, can be described by climatic indices.

The prevailing winds in Europe are the "Westerlies", blowing from the high pressure area in the subtropical latitudes towards the poles. The data in relation with the North Atlantic Oscillation (NAO) allow to check if any cycle affects the Westerlies. The scale spectra of the NAO indices (CRU & CPC) reveal the existence of a cycle corresponding to c_1 (see Fig. 8a). Since the influence of the NAO index is mainly visible in Western Europe (as shown for example by Hurrell (1995), this confirms the existence of a similar cycle in the temperature series obtained from Western European stations. Indeed, Paluš and Novotná (2006) have also observed a cycle corresponding to c_1 in the NAO CRU index and have shown the phase coherence between this cycle and the analogous period observed in a weather station located in Prague (Prague-Klementinum station).

Let us remark that the spectra associated to the NAO indices display a power law behavior with exponent $H-1 = -0.38 \pm 0.02$ (as showed in Fig. 9). It thus seems that these indices are perturbed by a colored Gaussian noise with long range correlations index equal to $H \approx 0.6$ (see Sect. 3.2).

At high and middle latitudes, the air mass flow over the Northern Hemisphere is in direct relation to the polar vortex, whose strength is characterized by the Arctic Oscillation (AO) index. The morphology of its scale spectrum, showed in Fig. 8b, is very similar, when looking at c_1 and c_2, to the morphology of the scale spectra of the global temperature time series in the Northern Hemisphere (Fig. 4), and is almost identical to the spectra of the series *CRUTEM3nh* and *CRUTEM3vnh*: both the cycles c_1 and c_2 are detected, but the maximum corresponding to c_2 is clearly dominated by the one corresponding to c_1. Since the zone of influence of the polar vortex spreads throughout over Europe and North Asia, it is quite natural to detect a

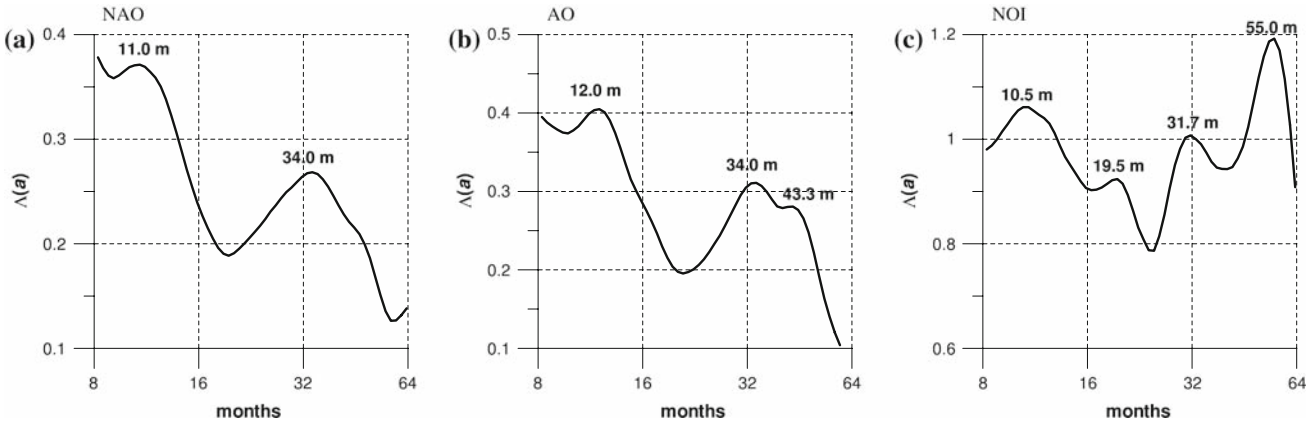

Fig. 8 Scale spectra of several Northern Hemisphere indices. **a** NAO (CPC). **b** AO (CPC). **c** NOI

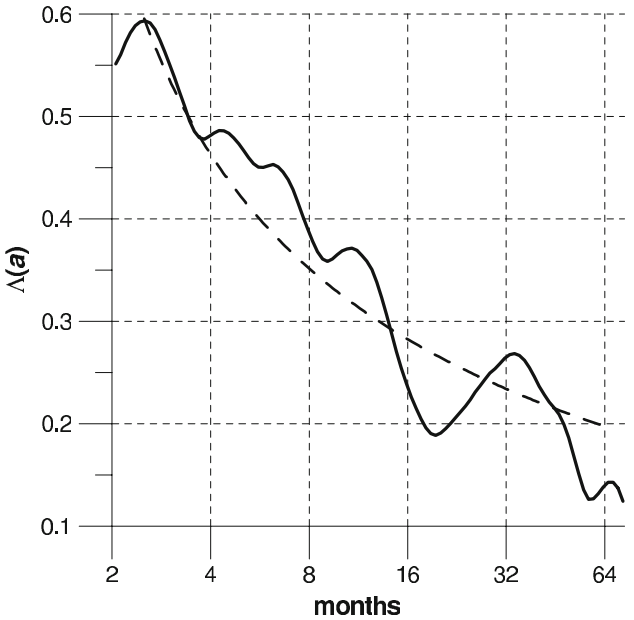

Fig. 9 The scale spectrum of the NAO CPC (*solid lines*) fitted with a power law. The resulting exponent is approximatively −0.4, attesting the presence of a colored Gaussian noise

cycle with the same period in the temperature time series obtained from these regions. This also corroborates the existence of the cycle detected in the Siberian stations.

As illustrated in Fig. 8c, the cycle c_1 is also found in the extratropical-based North Oscillation Index (NOI) which is driven by the atmospheric variability of the North Pacific Ocean. This reinforce the hypothesis of a strong relation between the climatic indices and the Northern Hemisphere temperatures.

The ENSO index is the main index used to describe the climatic variability in the Southern Hemisphere. The associated scale spectrum shows the existence of a cycle near c_2 (see Fig. 10a). This cycle was observed through the El Niño phenomenon by Fedorov and Philander (2000). Let us remark that the MEI ENSO index also displays the cycle c_1 (although it is much weaker than c_2), while Global-SST ENSO index does not. This can be easily understood, since the MEI ENSO index takes several parameters into account (e.g. air surface temperature, sea level pressure, zonal and meridional components of the surface wind...) that are expected to display the cycle c_1; in contrast, the Global-SST ENSO index is only defined using SST.

The Pacific Ocean behaves differently from the Atlantic Ocean, since the cycle c_2 is detected both in the temperature time series from the stations located near the Pacific Ocean and in the reanalyzed data. The North Pacific (NP), Pacific/North American (PNA) and Pacific Decadal Oscillation (PDO) indices reflecting the air mass flows over the North Pacific, also exhibit a maximum near c_2 (see Fig. 11). Concerning the South Pacific, the same argument can be applied to the Southern Oscillation Index (SOI*), whose spectrum also display a maximum located near c_2 (Fig. 10c). However, the spectrum of the SOI index clearly displays a bump corresponding to the cycle c_1, while the cycle c_2 is hardly seen (Fig. 10b). Let us say that, since this last index is computed with surface pressures obtained from stations only located in Darwin and Tahiti, it is more localized than the SOI* index. The oscillation associated to c_2 (also detected in the data related to the ENSO index) has a knock-on effect on some regions of the globe, in particular in South America, North America, South Africa, South Asia and near Australia, where the cycle c_2 is detected in the temperature time series.

The scale spectrum method has also been applied to the data obtained from the leading Empirical Orthogonal Functions (EOFs) of the Northern Hemisphere (20N–90 N) sea-level pressure monthly anomaly covariance. The first (EOF1), second (EOF2) and third (EOF3) components explain 17.9, 10.4 and 9.5% of the variance, respectively. The first component is the North Annular Mode (NAM) and is closely related to the NAO index; the second one is

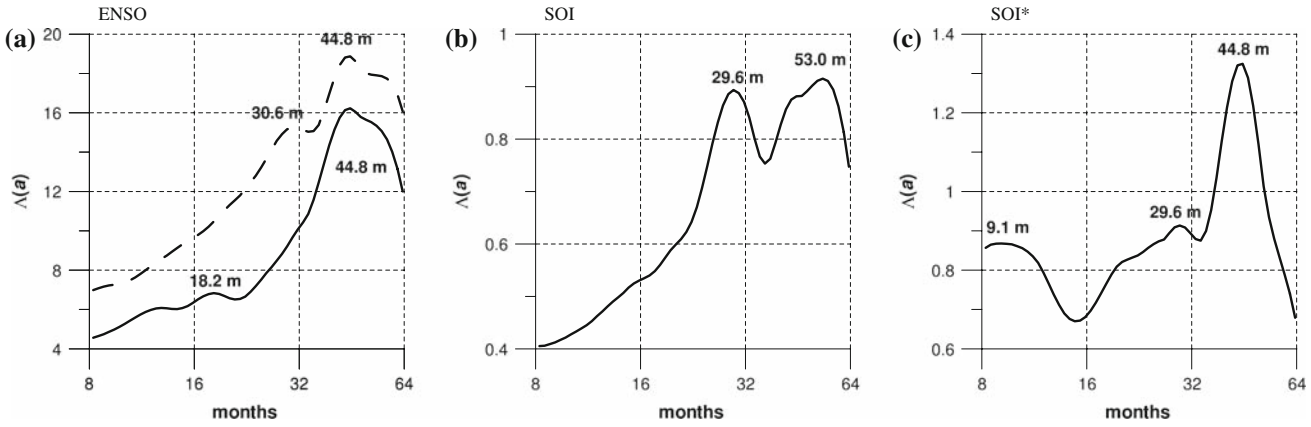

Fig. 10 Scale spectra of several indices related to the southern oscillation. **a** Global-SST ENSO (*solid lines*) and ENSO MEI (*dashed lines*). **b** SOI. **c** SOI*

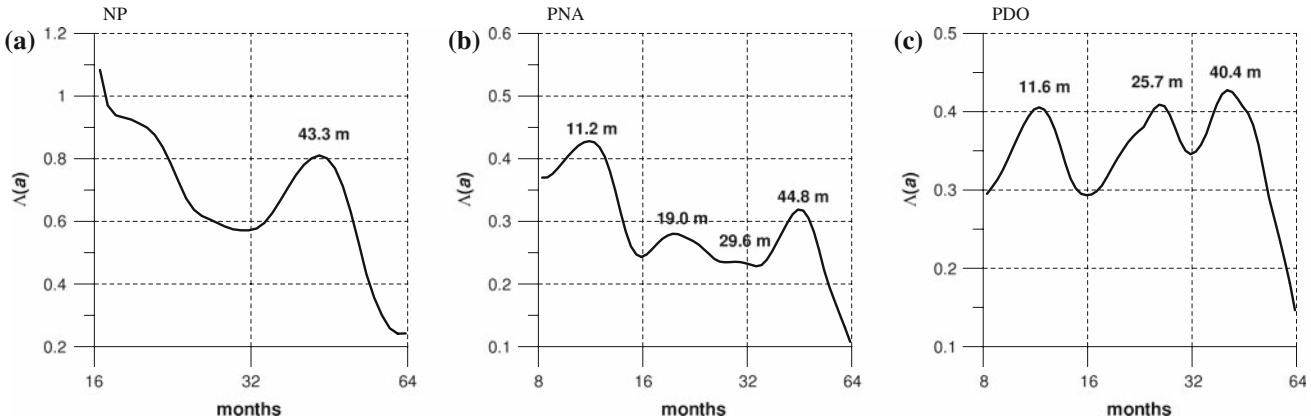

Fig. 11 Scale spectra of several indices related to the Pacific Ocean. **a** NP. **b** PNA (CPC). **c** PDO

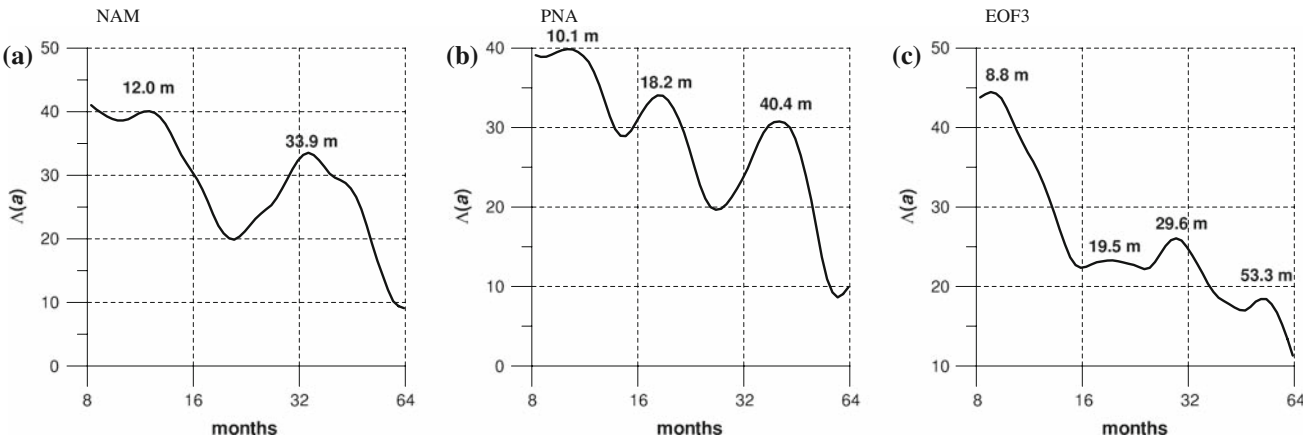

Fig. 12 Scale spectra of indices related to the EOFs. **a** NAM. **b** PNA. **c** EOF3

similar to the PNA index. As illustrated in Fig. 12, the cycle c_1 is clearly observed in EOF1 and EOF3. The regions of the globe under the influence of one of these components also display the cycle c_1. Let us remark that these regions are distinct, since EOF1 mainly covers the Western Europe and EOF3 mostly influences the Central Europe.

As expected, a maximum corresponding to a cycle of 29 months is observed in the spectrum of the Quasi-Biennial Oscillations (QBO) index, obtained from altitude

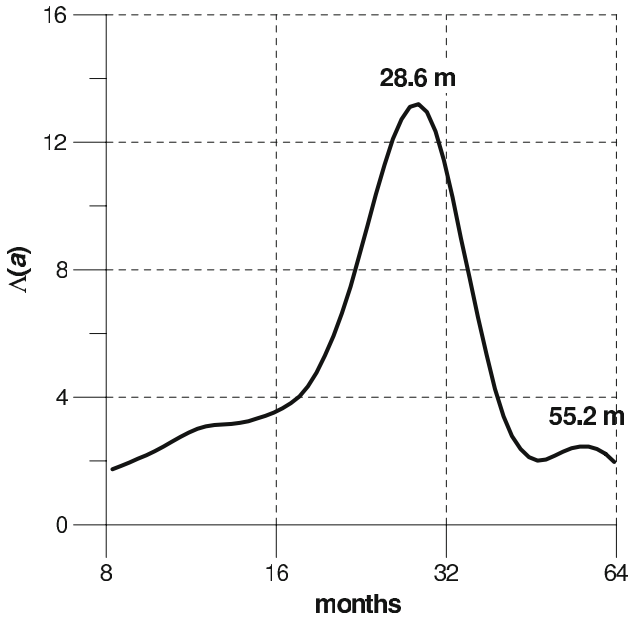

Fig. 13 Scale spectrum of the QBO index

data from Singapore (see Fig. 13). The temperature time series from Indonesia display the cycle c_1 that can be associated to the cycle of 29 months detected in the QBO index.

4.3 Scale spectra related to the solar activity

Since the cycles c_1 and c_2 are detected in temperature time series on the entire surface of the globe and since the climatic indices describing the air mass flows also display such cycles, a possible explanation is the solar activity variability.

The scale spectrum of the solar asymmetry shows the existence of a cycle close to c_2. The solar flux (the corrected and uncorrected data) and the solar asymmetry both display a maximum near 37 months (see Fig. 14).

The cycle of 37 months detected in the sun is a "flip–flop" type behavior: Following Mursula and Hiltula (2004), the solar rotation periodicity undergoes a phase reversal cycle. During the last 40 years, it is estimated, looking at the interplanetary magnetic field (IMF) components, to be about 3.2 years (see Takalo and Mursula 2002). This period is in good agreement with finding based on long series of sunspot observations obtained by Berdyugina and Usoskin (2003). As a matter of fact, the same period is detected in the scale spectrum of the sunspot number data.

Let us also remark that a cycle of 1 year, reflecting the influence of the Earth's move on the observations, is detected. Moreover, a cycle of period 25 months is detected in the sunspot number data; such a period has also been observed by Paluš and Novotná (2008) in addition to a cycle of period 43 months, not found when using our method. Therefore, no conclusion can be drawn concerning the existence of a relation between the sun and the periods c_1 and c_2 observed on earth.

5 Conclusions

The wavelet-based tool introduced in Sect. 3 provides a methodology for detecting "pseudo-cycles" in a noisy signal, even if it exhibits tendencies. The application to temperature records and climatic indices has lead to the detection of two pseudo-periods of 30 and 43 months approximatively (the detected cycles are given in Table 2). The cycle associated to 30 months is mainly seen all over Europe, while the cycle associated to 43 months is principally observed in North America. A previous work of Paluš and Novotná (2006) has already shown the existence of the cycle of period close to 30 months in Central Europe. The study of the climatic indices confirms these findings: the same cycles are detected in the indices and the

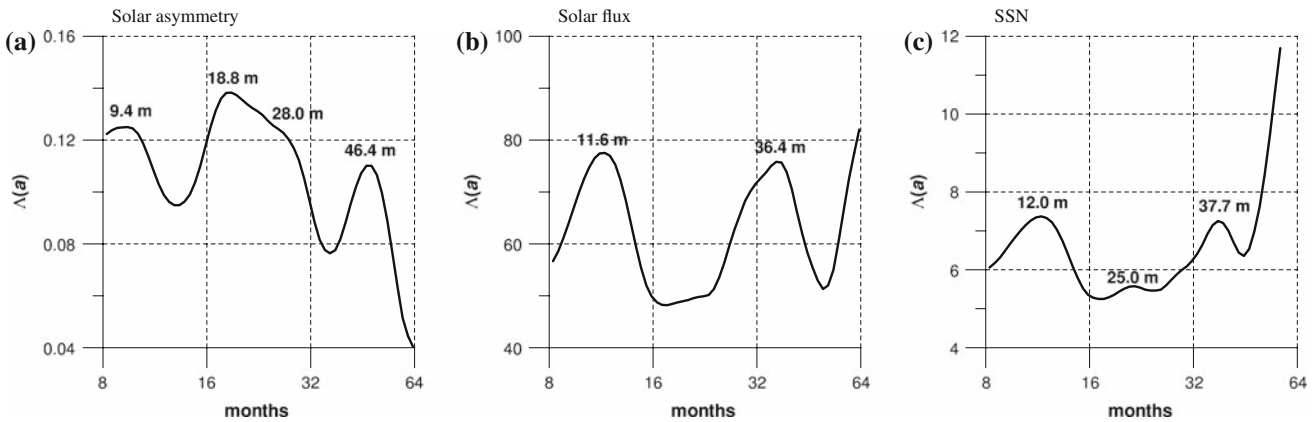

Fig. 14 Scale spectrum of the indices related to the solar activity. **a** Solar asymmetry. **b** Solar flux. **c** Sunspot number

Table 2 Summary of the cycles found in the dataset (rounded values)

time series	c_1	c_2
CRUTEM3gl	31 ± 2.6	42 ± 2.5
CRUTEM3vgl	30 ± 2.6	42 ± 2.6
HadCRUT3gl	31 ± 2.7	42 ± 2.7
HadCRUT3vgl	31 ± 2.7	42 ± 2.6
GLTs	30 ± 2.7	42 ± 2.7
HadSST2gl		42 ± 2.5
CRUTEM3nh	30 ± 2.5	40 ± 2.5
CRUTEM3vnh	30 ± 2.5	40 ± 2.5
HadCRUT3nh	29 ± 2.5	42 ± 2.6
HadCRUT3vnh	29 ± 2.5	40 ± 2.6
NHTs	30 ± 2.6	42 ± 2.6
HadSST2nh	29 ± 2.7	42 ± 2.5
CRUTEM3sh	32 ± 2.6	43 ± 2.7
CRUTEM3vsh	32 ± 2.6	43 ± 2.7
HadCRUT3sh	25 ± 2.7	43 ± 2.7
HadCRUT3vsh	25 ± 2.7	43 ± 2.6
SHTs)	28 ± 2.6	43 ± 2.7
HadSST2sh	25 ± 2.7	43 ± 2.7
Daily NAO (CPC)	34 ± 2	
Monthly NAO (CPC)	34 ± 2.1	
Monthly NAO (CRU)	34 ± 2.1	
Daily AO (CPC)	34 ± 2.9	43 ± 2.8
Monthly AO (CPC)	34 ± 2.6	43 ± 2.5
NOI	32 ± 2.3	
SOI	30 ± 2.2	
SOI*	30 ± 2.5	44 ± 2.6
PNA		45 ± 2.4
NP		43 ± 2.4
PDO	26 ± 2.4	40 ± 2.3
QBO	29 ± 2	
Global-SST ENSO		45 ± 2.1
MEI ENSO	30 ± 2.1	45 ± 2.1
Solar Flux ngdc daily	38 ± 2.8	
Solar Flux monthly	36 ± 2.8	
Solar Asymmetry		46 ± 2.8
Daily solar sunspot number	39 ± 2.5	
Monthly solar sunspot number	38 ± 2.5	

regions under the influence of these indices. Europe can be roughly associated with the NAO index (as also suggested by Paluš and Novotná 2006) and North America with the El Niño index. Although these data must be studied with caution, NCEP/NCAR reanalysis also corroborates the existence of these two cycles. A cycle of 37 months has also been detected in the solar data for the first time using such a spectral method; this observation is in good agreement with the previous experimental measurements of Takalo and Mursula (2002).

References

Arneodo A, Grasseau G, Holschneider M (1988) Wavelet transform of multifractals. PRL 61:2281–2287

Arneodo A, d'Aubenton Carafa Y, Bacry E, Graves P, Muzy J, Thermes C (1996) Wavelet based multifractal analysis of DNA sequences. Phys D 96:291–320

Arneodo A, Audit B, Decoster N, Muzy J, Vaillant C (2002) Climate disruptions, market crashes and heart attacks. In: Bunde A, Schellnhuber H (eds) The science of disasters. Springer, Berlin, pp 27–102

Baldwin MP et al (2001) The quasi-biennial oscillation. Rev Geophys 39:179–229

Barnston A, Livezey R (1987) Classification, seasonality and persistence of low-frequency atmospheric circulation patterns. Mon Weather Rev 115:1083–1126

Berdyugina SV, Usoskin IG (2003) Active longitutes in sunspot activity: century scale persistence. Astron Astrophys 405:1121

Brohan P, Kennedy JJ, Harris I, Tett SFB, Jones PD (2006) Uncertainty estimates in regional and global observed temperature changes: a new dataset from 1850. J Geophys Res 111:D12,106

Daubechies I (1992) Ten lectures on wavelets. SIAM, Philadelphia

Fedorov AV, Philander SG (2000) Is El Niño changing? Science 288:1997–2002

Goupillaud P, Grossman A, Morlet J (1984) Cycle-octave and related transforms in seismic signal analysis. Geoexploration 23:85–102

Hansen J, Ruedy R, JG, Sato M (1999) GISS analysis of surface temperature change. J Geophys Res 104:30,997–31,022

Hurrell JW (1995) Decadal trends in the North Atlantic Oscillation: regional temperatures and precipitation. Science 269:676–679

Jones P, Osborn TJ, Briffa KR, Folland CK, Horton EB, Alexander LV, Parker DE, Rayner NA (2001) Adjusting for sampling density in grid box land and ocean surface temperature time series. J Geophys Res 106:3371–3380

Kalnay E et al (1996) Ncep/Ncar 40-year reanalysis project. Bull Am Meteor Soc 77:437–471

Keller W (2004) Wavelets in geodesy and geodynamics. Gruyter, Berlin

Klein Tank AMG et al (2002) Daily dataset of 20th-century surface air temperature and precipitation series for the European climate assessment. Int J Climatol 22:1441–1453

Kronland-Martinet R, Morlet J, Grossmann A (1987) Analysis of sound patterns through wavelet transforms. Int J Pattern Recogn Artif Intell 1:273–302

Mallat S (1999) A wavelet tour of signal processing. Academic Press, New-York

Mantua NJ, Hare SR, Zhang Y, Wallace JM, Francis RC (1997) A pacific interdecadal climate oscillation with impacts on salmon production. Bull Am Meteorol Soc 78:1069–1079

Meyer Y (1989) Ondelettes et opérateurs. Hermann, Paris

Mursula K, Hiltula T (2004) Systematically asymmetric heliospheric magnetic field: evidence for a quadrupole mode and non-axissymmetry with polarity flip–flops. Sol Phys 224:133–143

Nelder J, Mead R (1965) A simplex method for function minimization. Comput J 7:308–313

Newton H, Milsom A (1955) Note on the observed differences in spottedness of the Sun's Northern and Southern Hemispheres. Monthly Not R Astron Soc 115:398:404

Nicolay S, Argoul F, Touchon M, d'Aubenton Carafa Y, Thermes C, Arneodo A (2004) Low frequency rhythms in human DNA sequences: a key to the organization of gene location and orientation? PRL 93:108,101

Paluš M, Novotná D (2008) Detecting oscillations hidden in noise: common cycles in atmospheric, geomagnetic and solar data. In: Donner R, Barbosa S (eds) Nonlinear time series analysis in

geosciences: applications in climatology, geodynamics and solar–terrestrial physics. Springer, Berlin, pp 327–353

Paluš M, Novotná D (2006) Quasi-biennal oscillations extracted from monthly NAO index and temperature records are phase-synchronized. Nonlinear Proc Geophys 13:287–296

Rayner NA, Brohan P, Parker DE, Folland CK, Kennedy JJ, Vanicek M, Ansell TJ, Tett SFB (2006) Improved analyses of changes and uncertainties in sea surface temperature measured in situ since the mid-nineteenth century: the HadSST2 dataset. J Clim 19:446–469

Schwing F, Murphree T, Green P (2002) The northern oscillation index (NOI): a new climate index for the northeast pacific. Prog Oceanogr 53:115–139

Takalo J, Mursula K (2002) Annual and solar rotation periodicities in IMF components: evidence for phase/frequency modulation. Geophys Res Lett 29:31–1–31–4

Trenberth K, Hurrell JW (1994) Decadal atmosphere–ocean variations in the pacific. Clim Dyn 9:303–319

Wolter K, Timlin MS (1993) Monitoring ENSO in coads with a seasonally adjusted principal component index. In: Proceedings of the 17th climate diagnostics workshop, Norman, OK, NOAA/N MC/CAC, NSSL, Oklahoma Clim Survey, CIMMS and the School of Meteor 52–57

Wolter K, Timlin MS (1998) Measuring the strength of ENSO events–how does 199798 rank. Weather 53:315–324

Zhang Y, Wallace JM, Battisti DS (1997) ENSO-like interdecadal variability. J Clim 10:1004–1020

Zhou S, Miller AJ, Wang J, Angell JK (2001) Trends of NAO and AO and their associations with stratospheric processes. Geophys Res Lett 28:4107–4110